Diffuse optical tomography system to image brain activation with improved spatial resolution and validation with functional magnetic resonance imaging

Danny K. Joseph, Theodore J. Huppert, Maria Angela Franceschini, and David A. Boas

Although most current diffuse optical brain imaging systems use only nearest-neighbor measurement geometry, the spatial resolution and quantitative accuracy of the imaging can be improved through the collection of overlapping sets of measurements. A continuous-wave diffuse optical imaging system that combines frequency encoding with time-division multiplexing to facilitate overlapping measurements of brain activation is described. Phantom measurements to confirm the expected improvement in spatial resolution and quantitative accuracy are presented. Experimental results showing the application of this instrument for imaging human brain activation are also presented. The observed improvement in spatial resolution is confirmed by functional magnetic resonance imaging. © 2006 Optical Society of America

OCIS codes: 170.0110, 170.3890, 170.3010.

1. Introduction

For more than two decades, near-infrared spectroscopy (NIRS) has been successfully used to monitor local changes in cerebral oxygenation and hemodynamics during functional brain activation in both adults and neonates.[1–5] With NIRS, cortical hemodynamics can be monitored noninvasively, continuously, in real time, and with compact and inexpensive instrumentation compared to positron emission tomography and functional magnetic resonance imaging (fMRI). NIRS can provide a temporal resolution of 10 to 100 Hz (depending on the signal-to-noise ratio). Furthermore, the difference in the near-infrared absorption spectra of oxyhemoglobin (HbO_2) and deoxyhemoglobin (HbR) allows the separate calculation of the concentrations of these two species from spectroscopic measurements.[6] The sum of the changes in the concentrations of oxyhemoglobin and deoxyhemoglobin additionally provides a measure of total hemoglobin concentration change [proportional to the cerebral blood volume change (ΔCBV)]. NIRS thus offers an advantage over the commonly used blood oxygen level dependent (BOLD) based fMRI technique, which is sensitive to changes in only the deoxyhemoglobin concentration.[7,8]

Diffuse optical tomography (DOT), however, has the disadvantage of relying on an ill-posed inverse problem to reconstruct an image of the hemodynamic response to brain activation.[9] The majority of activation images published to date have been produced by analysis of the hemodynamic response measured with nearest-neighbor pairs of sources and detectors and then an interpolation of the response between the measurement channels.[10–13] The resolution of these images is therefore comparable to the source–detector separation, which is typically 2–4 cm. In addition, the quantitative accuracy of the response is compromised because the image obtained is not an optimal solution of the inverse problem.[9] A suggested possible solution to these problems is the acquisition of overlapping sets of measurements.[14] Recently, we have shown that sources and detectors arranged in a hexagonal probe can provide overlapping measurements to improve spatial resolution by a factor of 2 while balancing the hardware demands of dynamic range and image temporal resolution.[14] In that work, the separations for the nearest and second-nearest source–detector pairs were 2.5 and 4.25 cm, respectively. This probe allowed a more uniform spatial sampling, which signif-

icantly reduced image artifacts directly beneath the source or detector positions for which single, nearest-neighbor measurements are insensitive.

We have observed that there is a 2 order of magnitude difference in light intensity detected from the adult brain at 2.5 and 4.25 cm distances on the head. Due to the limited instantaneous dynamic range (60–70 dB) of the detector channels in our imaging system, we could not obtain an acceptable signal-to-noise ratio for both the near and the far distance measurements with all the sources on the probe turned on simultaneously. We require 80 to 100 dB of dynamic range in the detection electronics for such measurements. In a previous work it was shown that by time-division multiplexing of sources and detector gains we could obtain such overlapping measurements with comparable signal-to-noise ratios.[14] In that case, the time-division multiplexing was done manually with three different subsets of measurements each lasting 600 s, where for each measurement subset different lasers were on with correspondingly appropriate detector gains. It is more desirable to acquire the different measurement subsets in 1 s or less to more accurately image the physiological fluctuation occurring within the brain.

Here we describe the development and characterization of a continuous wave system (CW-5) that combines frequency encoding of lasers with computer controlled time-division multiplexing of the lasers and detector gains to increase the effective dynamic range of each detection channel and to allow overlapping measurements while maintaining an image temporal resolution of ~1 Hz for functional brain imaging. Since this time-division multiplexing is now performed by the instrument control software, this system is capable of switching measurement subsets every 250 ms allowing three different measurement subsets to be collected in 1.2 s (accounting for delays in switching detector gains).

Schmitz *et al.*[15] have described a similar time-division multiplexed system. In that instrument, frequency multiplexing was limited to the different wavelengths, with only one source position being active at a given time thus requiring time-division multiplexing of all source positions. Instead, we frequency encode all 32 lasers in the system so that multiple source locations can be active at the same time. This allows us to acquire images at a rate of ~1 Hz. Our combination of frequency encoding with time-division multiplexing enables us to acquire the necessary effective dynamic range for overlapping measurements while maintaining an acceptable temporal resolution for functional imaging of ~1 Hz or better.

We first describe the time-multiplexed–frequency-encoded system in detail. We then present the characterization of the system with two dynamic phantoms: a homogeneous phantom for automated characterization of the CW-5 imaging system and a heterogeneous phantom that simulates brain activation. Finally, we experimentally demonstrate the afforded improvement in spatial resolution by imaging brain activation in adult humans. This improvement in spatial resolution is confirmed by spatial comparison with fMRI of brain activation in the same subjects.

2. Methods

A. System Design

1. Instrument Description

The continuous-wave imaging system (CW-5, TechEn Incorporated, Milford, Massachusetts) has 32 sources and 32 light detector channels. Figure 1 shows the photo of the CW-5 imaging system. Figure 2 is the block diagram of the signal flow from one source to one detector (for simplicity the other source and detector channels are not shown). The 10 MHz clock signal is derived from the master data acquisition card (National Instruments 6052E). The programmable square-wave generator was custom built using frequency division integrated circuits (TechEn Incorporated). Of the 32 laser sources, 16 are at 690 nm (Hitachi HL6738MG) and the other 16 are at 830 nm (Hitachi HL8325G). We typically set the 690 nm laser to a 12 mW average power and the 830 nm laser diode to a 6 mW average power. Each laser was modulated at a different frequency, from 6.4 to 12.6 kHz, with an interval of 200 Hz between adjacent frequencies. Each light detector channel consisted of an avalanche photodetector (APD) module (Hamamatsu C5460-01) followed by signal conditioning, amplification, and digitization stages (TechEn Incorporated). Each photodetector preamplifier output was first high-pass filtered to remove low frequency signals from stable interference sources like room light and $1/f$ noise generated by the electronics. The gain control stage amplified the signal voltage to match the voltage range of the data acquisition card and was programmable to vary the gain over a range of 65,000 with 16-bit control (custom built by TechEn Incorpo-
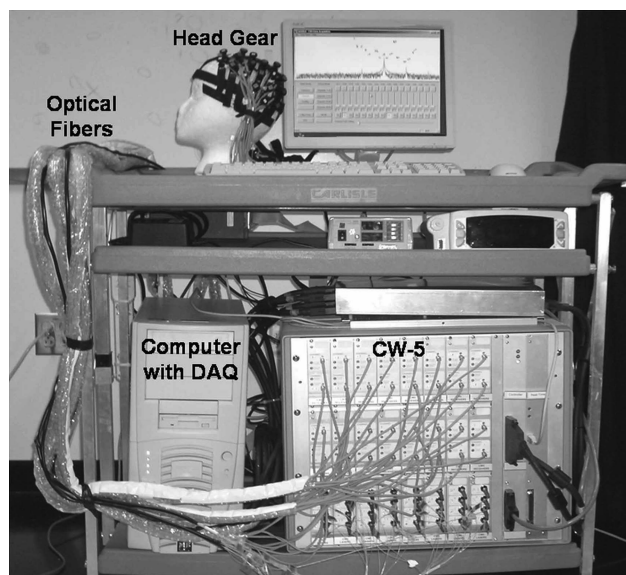

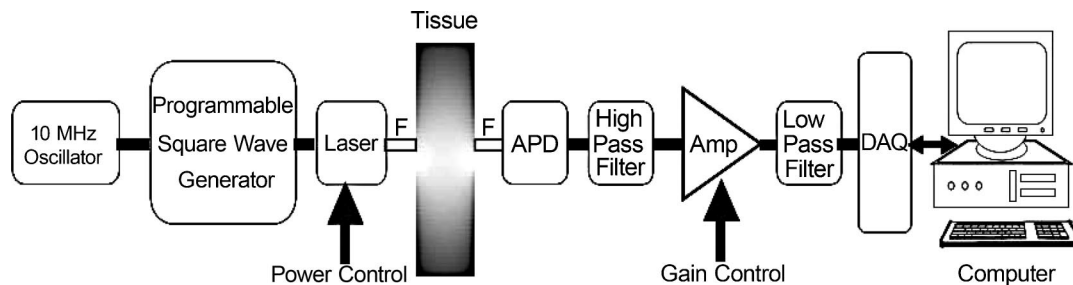Fig. 1. Photo of CW-5 imaging system and DAQ-data acquisition cards.

Fig. 2. Structure of the CW imager. Signal flow from one source to one detector: *F*, optical fiber; APD, avalanche photodetector module; Amp, amplifier; and DAQ is the data acquisition and control card.

rated). The low-pass filter was implemented to reduce aliasing during digital sampling. Each detector channel was then sampled at 41,666 samples/s. To sample all 32 detectors at this rate simultaneously, we use four National Instruments NI6052E data acquisition cards, each capable of acquiring eight differential channels at 333,333 samples/s. The continuous parallel operation of multiple sources and all the detectors allowed for rapid data collection.

Once the detected signals had been digitized, they were demodulated in software to determine the contribution at the detector attributable to each source channel. The structure of the in-phase and quadrature (IQ) digital demodulator program is shown in Fig. 3. All other spurious modulated optical signals (including those produced by line-powered lamps, computer terminals, or multiplexed LED displays), which are not phase-coherent to the source, exit the digital mixer in the form of frequency-shifted ac signals. A low-pass filter placed at the output of the mixer strongly attenuated these incoherent signals, leaving only the small dc voltage proportional to the magnitude of the source energy detected. The low-pass filter utilized a third-order Butterworth filter with a bandwidth of 20 Hz that was applied separately to the I and Q channels of the demodulator. The amplitude of the optical signal was subsequently derived from the square root of $I^2 + Q^2$.
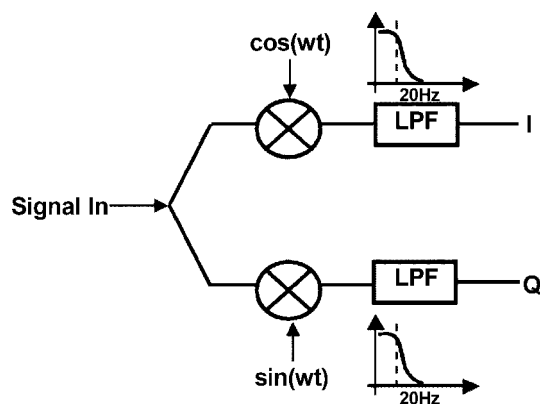

Fig. 3. Structure of the IQ digital demodulator program for demodulating one specific source. The signal is multiplied by the sine and cosine reference frequencies generated in the software, and then a Butterworth low-pass filter (LPF) (20 Hz bandwidth) is used to pickup the low frequency I and Q signals.

The imaging system had an auxiliary data collection unit to acquire physiology and stimulation trigger synchronously with the optical data. This unit used a National Instruments NI 6023E data acquisition card, which has eight input channels with each configured for a sampling rate of 25,000 samples/s.

The sources and detectors were connected to the head gear by using 0.4 mm diameter multimode fibers and 3 mm diameter fiber bundles, respectively. Fibers from a pair of lasers at 690 and 830 nm were epoxied together into a single optode to enable us to take spectroscopic measurements from the same position on the head. The head gear was made from flexible plastic and foam material and secured to a head band with Velcro.

2. Time-Division Multiplexing
In the hexagonal probe geometry shown in Fig. 4, the separations for the nearest- and second-nearest source–detector pairs are 2.5 and 4.25 cm, respectively. This geometry was chosen to optimize image quality and temporal resolution as described in Ref. 14. The detector channels (i.e., the APD, filters, gain stages, and data digitization) on the CW-5 imaging system do not have the required instantaneous dynamic range to maintain comparable signal-to-noise ratio at the shorter and longer separations simultaneously. To increase the effective dynamic range of the detector channels we used time-division multiplexing of the sources and the detector gains. Since the different sources had different frequencies we time-division multiplexed different sets of sources (rather than individual lasers) while optimal detector gains were synchronously set for each set of sources. For the hexagonal geometry this can be done with three states, specifically using sources 1, 5, 6; sources 2, 7; and sources 3, 4, 8. Software controls the switching of the sources and the detector gains, with detector gains typically increased by a factor of 10 to measure the further sources. Figure 5 shows the time traces of demodulated laser signals received by detector 1 in the three states from sources 6, 7, and 4, respectively. Each set of sources is on for 250 ms in each state. In addition there is a finite delay between different states due to the finite time to switch detector gains. This delay depends on the number of detector gains, which have to be changed from one state to another, and is slowed by
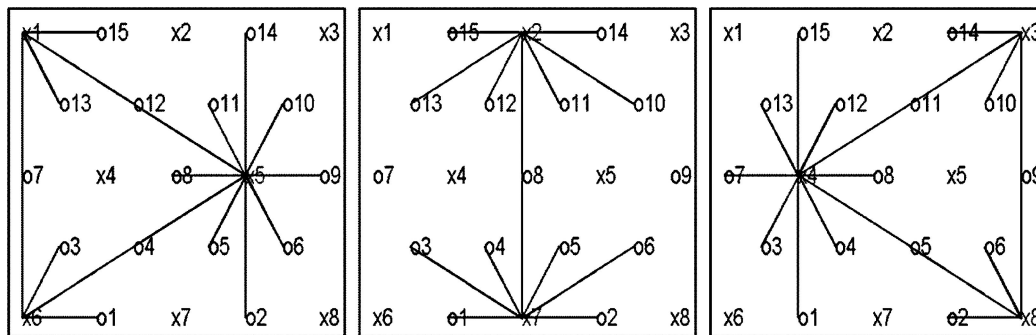
Fig. 4. State diagram with positions of sources (x's) and detectors (o's) indicated. The lines connect the active sources with the first- and second-nearest-neighbor detectors. Sources active in states 1, 2, and 3 are (1, 5 and 6), (2 and 7), and (3, 4, and 8), respectively.

the serial transmission of control data from the computer to the instrument. A complete cycle through the three states takes 1.2 s. An increase in the duty cycle can be achieved in the future by placing this digital control in the instrument itself rather than utilizing serial transmission from the computer. Note that the switching of lasers on and off results in missing data for individual source–detector pairs. We acquired data for each source–detector pair for 250 ms every 1.2 s, for a duty cycle of 21%. The missing data were interpolated.

B. System Characterization

An automated dynamic phantom was set up to allow the simultaneous characterization of all the detectors and lasers in the system. The phantom setup shown in Fig. 6 consists of a phantom box, syringe pump, cuvette, and a peristaltic pump. Lasers and detectors are connected to the phantom box in transmission geometry by using optical fibers. The syringe pump titrates black ink (absorber) uniformly into the reservoir filled with Intralipid solution (scattering medium). The peristaltic pump circulates this Intralipid and ink solution through the phantom box. At the beginning of the experiment the medium was weakly absorbing due to water absorption (i.e., no ink was present and the Intralipid had negligible absorption). The ink titration was initiated and continued until

the medium was strongly absorbing. The data were automatically collected from the detectors at regular 5 min intervals. In addition to measuring the source signals at each detector transmitted through the phantom, we also measured the transmission of light through a 3 mm thick cuvette in line with the circulating pump. The emitted and received light through the cuvette was collimated to detect only unscattered light. In this way, we could calculate the temporal changes in absorption of the medium given the initial scattering and absorption of the medium. Given the scattering and absorption properties of the medium and the evolution of absorption over time, we calculated the expected signal for each source and detector pair. The measured signal is compared with this predicted signal to estimate the linear dynamic range.

The heterogeneous phantom setup, which simulates brain activation, is shown Fig. 7 and consists of a phantom box, a sphere with a diameter of 3 cm, a cuvette, a peristaltic pump, and a syringe for injection of brain activation simulating absorber (black ink). The sphere was placed at various locations in the phantom box. The box was filled with an Intralipid and ink solution to mimic the optical properties of the human head at 830 nm (absorption coefficient of 0.05 cm^{-1} and reduced scattering coefficient of 10 cm^{-1}). A matched Intralipid solution was circulated through the sphere using the peristaltic pump. At regular intervals an ink bolus was injected into the sphere. This created a transient absorption increase in the sphere similar to brain activation. The lasers and detectors were con-
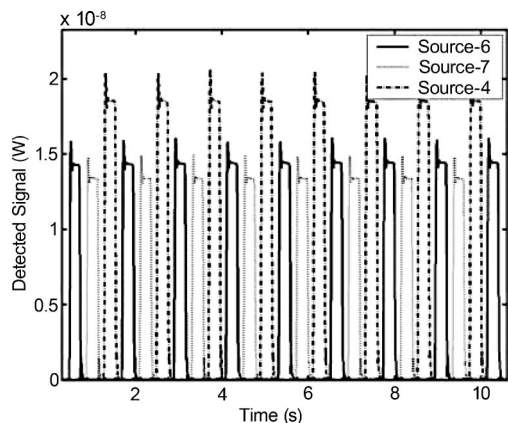

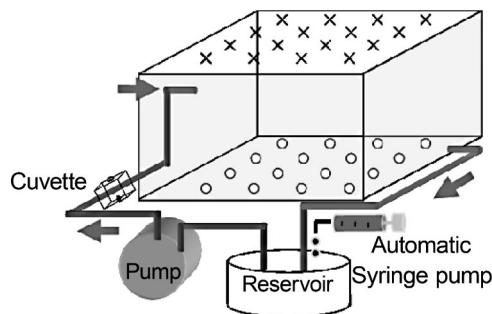Fig. 5. Demodulated laser signals received by detector 1 from sources 6, 7, and 4.

Fig. 6. Homogeneous dynamic phantom for system characterization. Positions of sources (x's) and detectors (o's) are indicated.
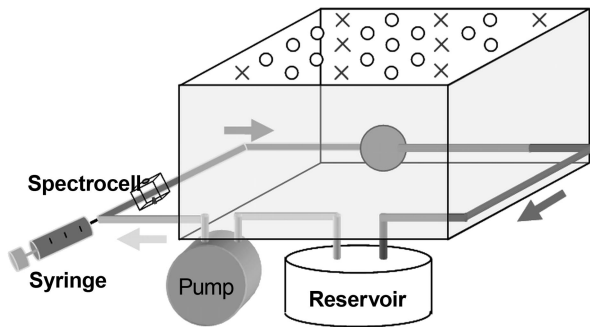
Fig. 7. Heterogeneous dynamic phantom that simulates brain activation. The positions of the sources (x's) and detectors (o's) are indicated.

nected to the phantom box using optical fibers and they were arranged in the hexagonal geometry. The cuvette was monitored by a single source and detector in transmission and served as a reference measurement of the ink bolus.

C. Validation for Brain Function Imaging

1. Human Subject Protocol

We performed measurements on human subjects to confirm the improvement in optical image quality by comparison with fMRI. We enrolled three healthy subjects (two male, one female). The Massachusetts General Hospital Institutional Review Board approved the study, and the subjects gave written informed consent.

The stimulation protocol consisted of multiple runs of an event-related finger-tapping task with on periods of 2 s. The interstimulus interval (ISI) between finger-tapping periods was pseudorandomly chosen and optimized to provide the uniform temporal coverage necessary for deconvolution with a 500 ms time step.[16] The length of the ISI ranged between 4 and 20 s with an average ISI period of 12 s. Each run lasted for 6 min and the subjects participated in five such runs. At the end of the study the position of the optodes was recorded by using a 3D digitizer (Polhemus) with nasal, left, and right ear points as reference. This information was used to coregister the location of brain activation identified by DOT with MRI.

2. Optical Data Processing and Visualization

The individual source signals were demodulated and low-pass filtered with a bandwidth of 20 Hz. The missing data points corresponding to the time when a source was off were linearly interpolated from neighboring known data points. The rest of the data processing and visualization was done with a custom MATLAB data analysis program (HomER), which is available for public download and use (see Ref. 17). Signals were further low-pass filtered at 0.2 Hz using a zero-phase forward and reverse digital filter to remove the heart signal. Changes in optical density for each source–detector pair were then high-pass filtered with a 1/30 Hz drift correction. From optical density data, the individual subject's hemodynamic re-

sponses were calculated for each wavelength by using a least-squares linear deconvolution[18] and implemented within the HomER program. Regions of time showing significant motion artifacts (as clearly evidenced by extremely large and sudden perturbations in the measurement time course) were rejected from the analysis. The hemodynamic response functions were then averaged for each source–detector pair over 135 responses across all five runs for each subject. We reconstructed images of absorption changes at the two wavelengths from the hemodynamic response function data averaged across the duration of activation (i.e., the response for each source–detector pair was averaged from 2 to 8 s where 0 s is the time at which the 2 s stimulus began). Images of absorption changes were finally converted to changes in hemoglobin concentrations.

For image reconstruction, we used the linear Rytov approximation to the photon diffusion equation to image changes in the measured photon fluence from spatial changes in the absorption coefficient,[9] that is,

$$\mathbf{y} = A\mathbf{x}, \tag{1}$$

where the jth element of vector $\mathbf{x}$ indicates the absorption perturbation at the jth voxel, and the ith element of vector $\mathbf{y}$ represents the variation in the ith measurement that is due to spatial variation of the absorption coefficient x from background absorption. Matrix A is the linearized transformation from image space x to measurement space y.

For the case in which there are fewer measurements than unknowns the linear problem is underdetermined and is given by the (regularized) Moore–Penrose generalized inverse

$$\hat{x} = A^{\mathrm{T}}(AA^{\mathrm{T}} + \lambda I)^{-1}y, \tag{2}$$

where I is the identity matrix, λ is the Tikhonov regularization parameter, and y is the measured data.

In the results given here, we chose $\lambda = 10^{-1}$ of the maximum eigenvalue of AA^{T}.[19] We refer to this reconstruction scheme as the DOT reconstruction and use this to reconstruct images from the multidistance measurements. When images are reconstructed using only single distance measurements we use a column normalized backprojection scheme[20] given by

$$\hat{x} = (AS)^{\mathrm{T}}y, \tag{3}$$

where the diagonal matrix S produces column normalization(one norm) of matrix A.

3. Functional Magnetic Resonance Imaging Protocol

BOLD-fMRI measurements were performed using a 3 Tesla Siemens Allegra MR scanner (Siemens Medical Systems, Erlangen, Germany). Data were taken with the (gradient) echo planar imaging sequence (TR/TE/θ = 500 ms/30 ms/90°) with five 6 mm slices (1 mm spacing) and 3.75 mm in-plane spatial

Table 1. Performance Characteristics of CW-5

Parameter	Value
Dynamic range (bandwidth)	68 dB (20 Hz)
Noise equivalent power	0.05 pW/root hertz
Drift	<0.5% over 5 min

resolution. Structural scans were performed using a T1-weighted magnetization prepared rapid gradient echo (MPRAGE) sequence (1 mm × 1 mm × 1.33 mm resolution, TR/TE/θ = 2.53 s/3.25 ms/7°).

To calculate the BOLD-based hemodynamic response functions, the functional images were first motion corrected[21] and spatially smoothed with a 6 mm Gaussian kernel. The hemodynamic response functions were then calculated by a least-squares linear deconvolution. A third-order polynomial was included to remove drift effects. As with the NIRS analysis, the hemodynamic response was estimated without assumptions of fixed canonical responses and was averaged from 2 to 8 s following the start of the 2 s duration stimulus.

4. Coregistration and Functional Magnetic Resonance Imaging Projection

To register the optical and BOLD images for spatial comparison, the optode positions from the Polhemus 3D digitizer were registered to the anatomical MPRAGE images using the three fiducial head

points for orientation by rigid-body affine transformation. These three points were manually selected in the MPRAGE volumes. Since the digitized locations had been marked by the Polhemus digitizer on the top surface of the optode, rather than the surface of the subject's head, the resulting optode locations from this rotation were elevated above the head's surface. These positions were brought to the surface of the head using a nonlinear relaxation algorithm. This algorithm utilized an energy cost function based on a series of connected, virtual, elastic springs between the optode positions:

$$E_i = \frac{1}{2} \mathcal{K}(x_i - \hat{x}_i)^2, \tag{4}$$

where E_i is the energy of the ith connection between a source and a detector, $\mathcal{K}$ is an adjustable spring constant, and $\hat{x}_i$ is the interoptode distance for this conection, which was precomputed from the physical design of the probe layout. Only nearest-neighbor connections were used in the energy cost function. The algorithm brought the optodes to the head's surface, while minimizing the above cost function in an iterative manner. Following registration, the fMRI data were projected from the cortex to a scalp surface image using an equal-area map projection algorithm through the center of the optical probe.[22] For fMRI images, the functional contrast projected to the scalp was averaged from 2 to 8 s poststimulus onset.
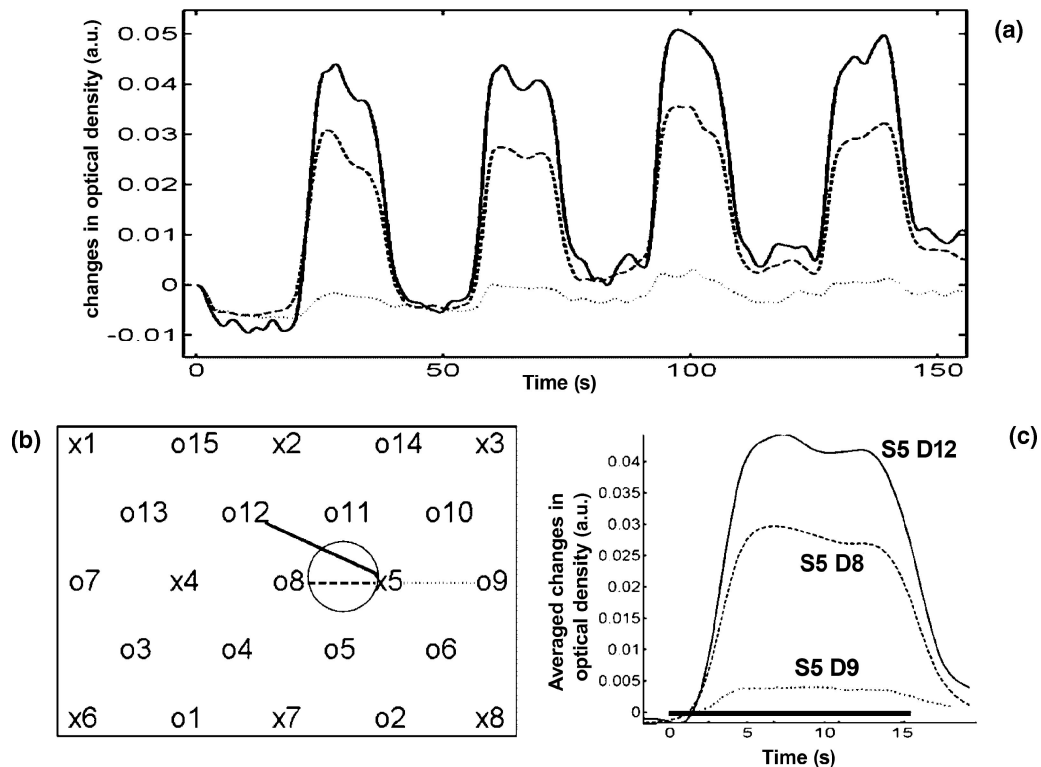

Fig. 8. Time course for brain activation simulating phantom. (a) Time courses with increase in optical density (decrease in light amplitude) for detectors 12, 8, and 9 with light received from source 5, (b) probe geometry where the circle corresponds to the projection of the spherical inhomogeneity on the probe, and (c) time courses of the averaged change in optical density for detectors 12, 8, and 9. The black bar corresponds to the period of injection of ink bolus.

3. Results

A. System Characterization

The parameters that characterize the continuous-wave system are the stability of the lasers, and the dynamic range and noise-equivalent power of the detectors. Using the homogeneous dynamic phantom setup we can observe the performance of a detector over the entire dynamic range from saturation to the noise floor. Table 1 quantifies the key characterization parameters of CW-5.

The dynamic range of the instrument is defined by the ratio of the light that saturates the detector channel at high signal levels and the noise equivalent power at low signal levels. For the different detector channels in the CW system, the dynamic range varied between 60 and 70 dB with a less than 2% deviation from a linear least-squares fit.

When detecting low light with an APD module, the signal-to-noise ratio is determined by shot noise by signal light and noise generated in the current-to-voltage conversion amplifier. The shot noise by signal light is nearly proportional to the square root of the signal light. When the signal level is low, the noise is dominated by the amplifier noise and is independent of signal. The noise-equivalent power (NEP) corresponds to the amount of light that, when incident on the APD module, has a signal-to-noise ratio of unity. This is calculated as 0.05 pW per root hertz, which is comparable to the NEP specified for the APD module
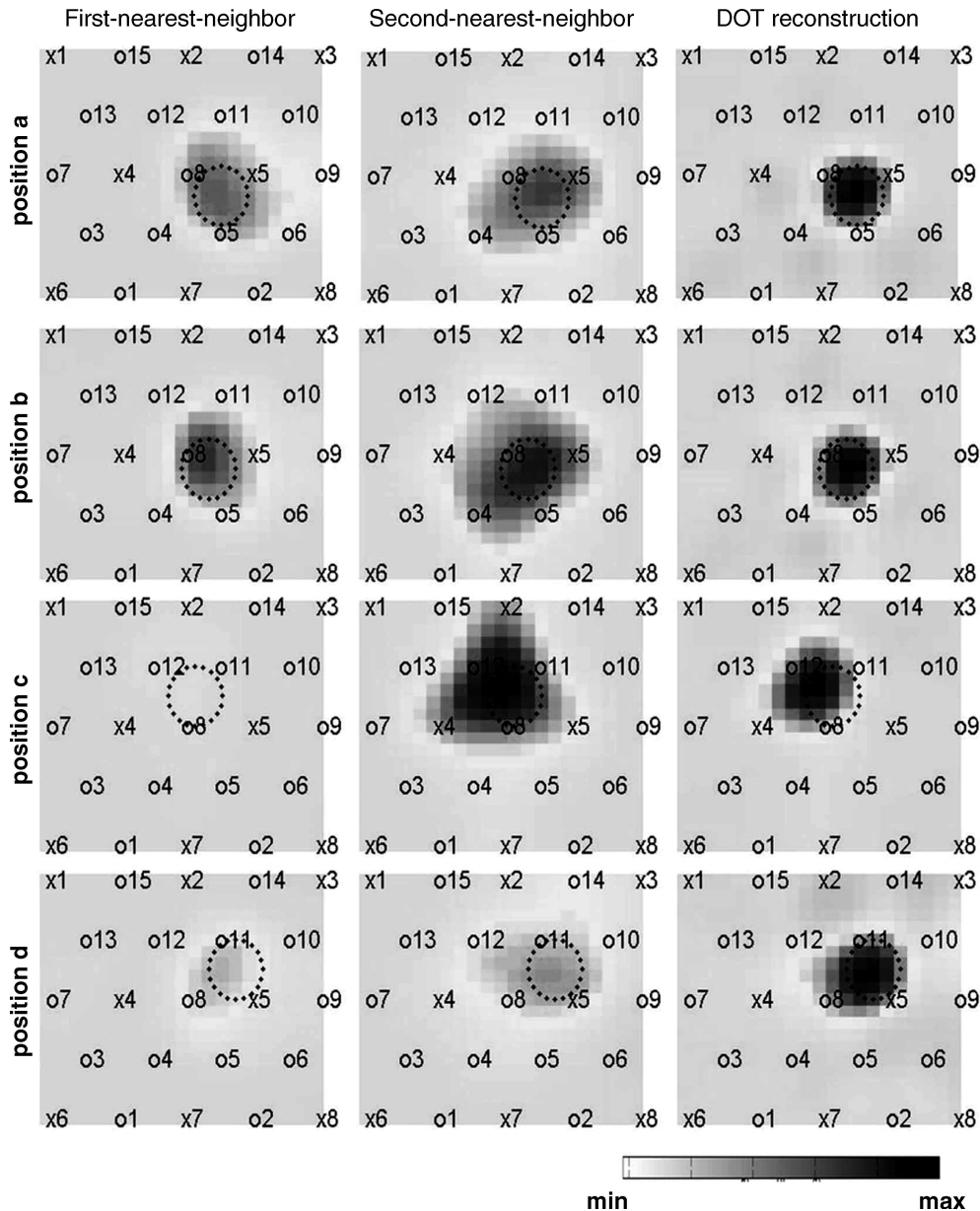

Fig. 9. Comparison of backprojection images obtained from first- and second-nearest-neighbor measurements with the DOT image for the brain activation simulating phantom. The positions of sources (x's) and detectors (o's) are indicated by the numbers in the reconstructed images. The dotted circle corresponds to the actual projection of the sphere centered 2.6 cm below the probe.
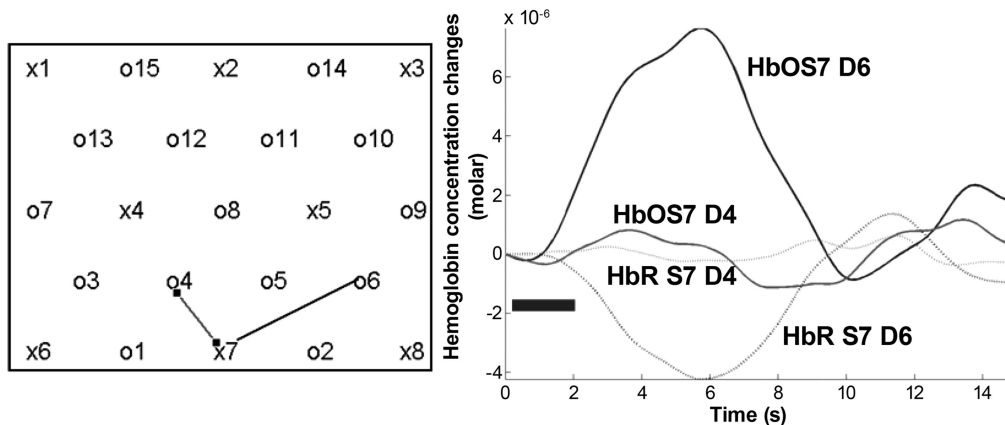
Fig. 10. Temporal Profile of hemodynamic activity for subject A. HbO, oxyhemoglobin; HbR, deoxyhemoglobin; S, source; and D, detector. The curve labeled HbO S7 D6 displays the Beer–Lambert estimate of oxyhemoglobin concentration change measured between source 7 and detector 6 and averaged across all 5 runs.

(C5460-01, Hamamatsu). This indicated that the circuitry following the APD module preserves the signal-to-noise ratio achieved by the APD module.

The stability of the signal from each detector channel for each laser was measured to be less than 0.5% drift over 5 min (after 30 min of system warmup). During time-division multiplexing where the lasers are turned on and off and the detector gains are modulated during data collection, the drift was less than 0.8% over 5 min.

B. Validation Studies

1. Measurements on Heterogeneous Phantom
Figure 8(a) shows the time course for changes in optical density (OD $= \log_{10} I/I_o$) for near-infrared light (830 nm) from source 5 incident at detectors 8, 9, and 12, respectively, when the ink bolus is injected five times at 22, 60, 95, 132, and 165 s. Each bolus lasts approximately 20 s. The spherical absorption inhomogeneity has a diameter of 3 cm and is centered at a depth of 2.6 cm. The circle in Fig. 8(b) shows the projection of the sphere on the probe. The block averaged change in OD for different source–detector combinations is shown in Fig. 8(c).

The images reconstructed at a depth of 2.5 cm are shown in Fig. 9 with each row corresponding to a different position of the sphere. The three columns correspond, respectively, to the backprojection images with only nearest-neighbor measurements, the backprojection images with only the second-nearest-neighbor measurements, and the DOT images reconstructed with both the nearest and the second-nearest neighbors.

It could be observed that for all the sphere positions the location and width or diameter of the inhomogeneity reconstructed by DOT better matches the true projection of the sphere (dotted circle) compared to the backprojection images. Also, for the sphere positions in Figs. 9(c) and 9(d) the inhomogeneity is not well resolved when the image is reconstructed by backprojection with just the nearest-neighbor measurements because it is located in a region not sampled by nearest-neighbor measurements. These results are in agreement with the quantitative analysis of spatial resolution and image accuracy presented in Ref. 14.

2. Optical Imaging of Adult Brain Activation
In the three subjects we recorded optical signals containing noise that was less than 1% of the signal. Figure 10 shows a temporal plot of the hemodynamic activation measured on the first subject. Oxyhemoglobin concentration increases and deoxyhemoglobin decreases in response to the finger-tapping task between source 7 and detector 6. A neighboring region, between source 7 and detector 4, is plotted in the graph to show the lack of hemoglobin changes in this area.

3. Comparison with Functional Magnetic Resonance Imaging
In Figs. 11, 12, and 13 we qualitatively compare deoxyhemoglobin maps reconstructed from optical data with projected fMRI images for the three different
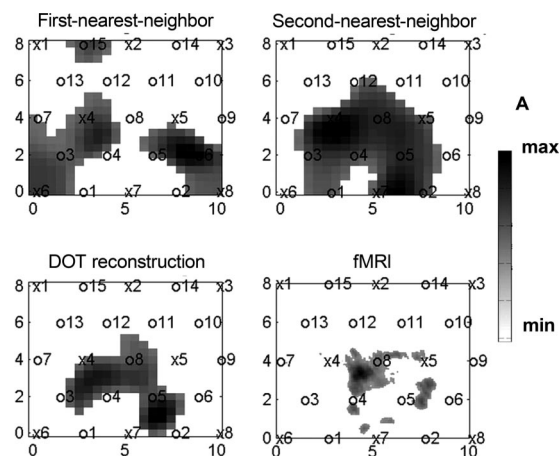

Fig. 11. Qualitative comparison of deoxyhemoglobin maps reconstructed from optical data by the different image reconstruction algorithms with projected fMRI images for subject A. The positions of the sources (x's) and detectors (o's) are indicated by the numbers in the reconstructed images.
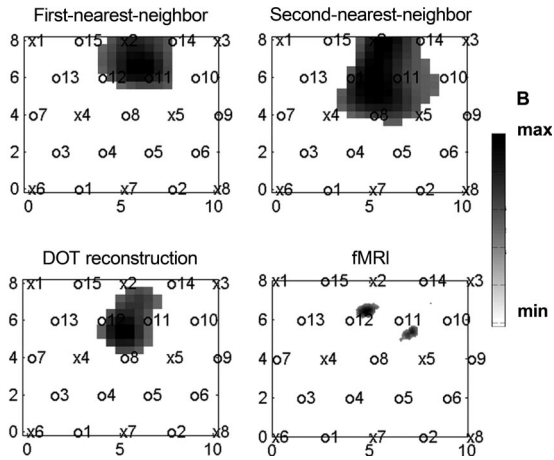
Fig. 12. Qualitative comparison of deoxyhemoglobin maps reconstructed from optical data by the different image reconstruction algorithms with projected fMRI images for subject B. The positions of sources (x's) and detectors (o's) are indicated by the numbers in the reconstructed images.

subjects. We display images for both the optical and the fMRI images at a half-maximum threshold to validate the improvement in the spatial resolution of the optical image that is afforded by the overlapping measurements. The spatial extent of the brain activation is compared for four images: the fMRI, the nearest-neighbor backprojection, the second-nearest-neighbor backprojection, and the DOT reconstruction of the overlapping data. From these images it appears that the optical image generally localizes the brain activation in the same general region as the fMRI, with differences that can arise from the differing depth sensitivity of the optical and fMRI methods. Qualitatively, from the three examples, it is clear that the DOT images provide a more localized image than the backprojection images consistent with the phantom experiments and that the DOT images more
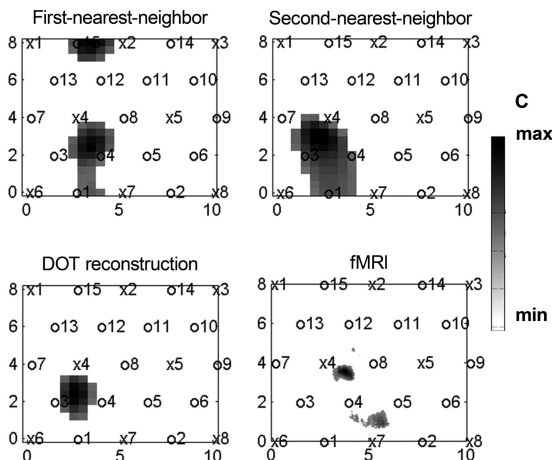

Fig. 13. Qualitative comparison of deoxyhemoglobin maps reconstructed from optical data by the different image reconstruction algorithms with projected fMRI images for subject C. The positions of sources (x's) and detectors (o's) are indicated by the numbers in the reconstructed images.

Table 2. Area of Brain Activation

| | | | Area of Brain Activation (Square cm) Identified by | |
| | | | First-nearest Neighbor Backprojection | Second-nearest Neighbor Backprojection |
Subject	fMRI	DOT		
A	9	19	33	40
B	2	9	11	22
C	1	4	10	12

closely match the fMRI images. This improvement is quantified in Table 2, which presents the spatial extent of brain activation in square centimeters. The area was determined by the number of activated pixels that exceed the half-maximum threshold.

4. Summary

We have implemented a DOT system that combines frequency encoding with time-division multiplexing to increase the effective dynamic range of the detectors to allow overlapping measurements while maintaining an image temporal resolution of ~1 Hz as appropriate for functional brain imaging. The system was described in detail along with phantom and human subject brain activation experiments to demonstrate the improvement in image sensitivity and resolution afforded by overlapping measurements. We have confirmed, by comparison with fMRI, the improved spatial resolution afforded by this system by using overlapping measurements with respect to the simple single-distance backprojection scheme. The fMRI shows a smaller region of brain activation than that observed by optical imaging, indicating that further improvements in optical image resolution are needed. Further improvements in spatial resolution can arise either from a greater density of optical measurements and/or from incorporating prior information into the optical image reconstruction. To improve temporal resolution, we can reduce the data acquisition dead time during which control information is serially sent from the computer to the instrument. This can be accomplished by passing control of the detector gains to a processor in the instrument rather than relying on the external computer.

References

1. Y. Hoshi, "Functional near-infrared optical imaging: utility and limitations in human brain mapping," Psychophysiology **40,** 511–520 (2003).
2. M. Ferrari, L. Mottola, and V. Quaresima, "Principles, Techniques, and limitations of near infrared spectroscopy," Can. J. Appl. Physiol. **29,** 463–87 (2004).
3. A. Villringer, J. Planck, C. Hock, L. Schleinkofer, and U.

Dirnagl, "Near infrared spectroscopy: new tool to study hemodynamic changes during activation of brain function in human adults," Neurosci. Lett. **154,** 101–104 (1993).

4. G. Gratton, M. Fabiani, D. Friedman, M. A. Franceschini, S. Fantini, P. M. Corballis, and E. Gratton, "Rapid changes of optical parameters in the human brain during a tapping task," J. Cogn. Neurosci. **7,** 446–456 (1995).

5. B. Chance, Z. Zhuang, U. A. Chu, C. Alter, and L. Lipton, "Cognition activated low frequency modulation of light absorption in human brain," Proc. Natl. Acad. Sci. U.S.A. **90,** 2660–2774 (1993).

6. M. Cope and D. T. Delpy, "System for long-term measurement of cerebral blood flow and tissue oxygenation on newborn infants by infrared transillumination," Med. Biol. Eng. Comput. **26,** 289–294 (1988).

7. S. Ogawa, D. W. Tank, R. Menon, J. M. Ellermann, S. G. Kim, H. Merkle, and K. Ugurbil, "Intrinsic signal changes accompanying sensory stimulation: functional brain mapping with magnetic resonance imaging," Proc. Natl. Acad. Sci. U.S.A. **89,** 5951–5955 (1992).

8. K. K. Kwong, J. W. Belliveau, D. A. Chesler, I. E. Goldberg, R. M. Weisskoff, B. P. Poncelet, D. N. Kennedy, B. E. Hoppel, M. S. Cohen, R. Turner, H. Cheng, T. J. Brady, and B. R. Rosen, "Dynamic magnetic resonance imaging of human brain activity during primary sensory stimulation," Proc. Natl. Acad. Sci. U.S.A. **89,** 5675–5679 (1992).

9. S. R. Arridge, "Optical tomography in medical imaging," Inverse Probl. **15,** R41–R93 (1999).

10. A. Maki, Y. Yamashita, Y. Ito, E. Watanabe, Y. Mayanagi, and H. Koizumi, "Spatial and temporal analysis of human motor activity using noninvasive NIR topography," Med. Phys. **22,** 1997–2005 (1995).

11. M. A. Franceschini, V. Toronov, M. Filiaci, E. Gratton, and S. Fantini, "On-line optical imaging of the human brain with 160 ms temporal resolution," Opt. Express **6,** 49–57 (2000).

12. D. A. Boas, T. J. Gaudette, G. Strangman, X. Cheng, J. J. A. Marota, and J. B. Mandeville, "The accuracy of near infrared spectroscopy and imaging during focal changes in cerebral hemodynamics," Neuroimage **13,** 76–90 (2001).

13. G. Gratton, P. M. Corballis, E. Cho, M. Fabiani, and D. C. Hood, "Shades of gray matter: noninvasive optical images of human brain responses during visual stimulation," Psychophysiology **32,** 505–9 (1995).

14. D. A. Boas, K. Chen, D. Grebert, and M. A. Franceschini, "Improving the diffuse optical imaging spatial resolution of the cerebral hemodynamic response to brain activation in humans," Opt. Lett. **29,** 1506–1508 (2004).

15. C. H. Schmitz, M. Locker, J. M. Lasker, A. H. Hielscher, and R. L. Barbour, "Instrumentation for fast functional optical tomography," Rev. Sci. Instrum. **73,** 429–439 (2002).

16. A. M. Dale, "Optimal experimental design for event-related fMRI," Human Brain Mapp. **8,** 109–114 (1999).

17. Photon Migration Imaging Lab, Martinos Center for Biomedical Imaging, http://www.nmr.mgh.harvard.edu/PMI/.

18. J. T. Serences, "A comparison of methods for characterizing the event-related BOLD time series in rapid fMRI," Neuroimage **21,** 1690–1700 (2004).

19. H. Dehghani, D. C. Barber, and I. Basarab-Horwath, "Incorporating *a priori* anatomical information into image reconstruction in electrical impedance tomography," Physiol. Meas **20,** 87–102 (1999).

20. A. C. Kak and M. Slaney, *Principles of Computerized Tomographic Imaging* (IEEE Press, 1988).

21. R. W. Cox and A. Jesmanowicz, "Real-time 3D image registration for functional MRI," Magn. Reson. Med. **42,** 1014–1018 (1999).

22. E. W. Weisstein, "Lambert azimuthal equal-area projection," *MathWorld,* http://mathworld.wolfram.com/LambertAzimuthal-Equal-AreaProjection.html.